# First-principles theory for Schottky barrier physics

Dmitry Skachkov [ORCID],[*] Shuang-Long Liu [ORCID], Yan Wang [ORCID],[†] Xiao-Guang Zhang [ORCID],[‡] and Hai-Ping Cheng [ORCID]
*Center for Molecular Magnetic Quantum Materials, University of Florida, Gainesville, Florida 32611, USA*
*and Department of Physics and the Quantum Theory Project, University of Florida, Gainesville, Florida 32611, USA*

We develop a first-principles theory for Schottky barrier physics. The Poisson equation is solved self-consistently with the electrostatic charge density over the entire barrier using the density functional theory (DFT) electronic structure converged locally, allowing computation of a Schottky barrier entirely from DFT involving thousands of atomic layers in the semiconductor (SC). The induced charge in the bulk consists of conduction and valence band charges from doping and band bending, as well as charge from the evanescent states in the gap of the SC. The Schottky barrier height (SBH) is determined when the induced charge density and the induced electrostatic potential reach self-consistency. Tests on the GaAs-graphene and Si/Al heterostructures yield SBH, width, along with depletion and inversion layers obtained self-consistently as functions of temperature and bulk doping.

## I. INTRODUCTION

The physical property of a Schottky contact is one of the most important topics in semiconductor (SC) physics because metal-SC contacts are the main components of SC electronic devices [1–8]. Schottky barriers form at the interface between a SC and a metal or between two dissimilar SCs. At such an interface, charge transfer between the two materials is necessary to bring their Fermi levels into alignment. However, in a SC, the Fermi level density of states (DOS) is nominally zero, requiring a space charge layer of macroscopic thickness to accommodate the amount of charge transfer needed. A corresponding shift in the electrostatic potential produces a potential barrier for the carriers [9,10]. The physics of the Schottky barrier is rich and has far-reaching impacts. It is important in wide-ranging problems including how to make good contact between the SC and the metal layer to avoid surface charge accumulation and produce high-quality Schottky contacts [11,12] and how to use gate dielectrics to avoid Fermi level pinning [13,14] and reduce tunneling from metal to SC [15–18]. A Schottky barrier is characterized by the barrier height and thickness, both of which depend on many factors, for example, the quality and structure of the SC surface [19–22], electronic structure of the surface [6], and the lattice strain [23].

The macroscopic size of a Schottky barrier typically exceeds thousands of atomic layers of the SC and makes its self-consistent computation from first-principles a prohibitively difficult task. Lacking a fully self-consistent density

functional theory (DFT) solution for the entire barrier region, DFT studies focused on the problem of band alignment [10,24–36], which is usually determined by comparing characteristic energy levels or core electron levels at the interface with that in the bulk SC [37,38], or on averaging the electrostatic potential [29,32]. Such calculations typically require separate interface and bulk calculations, with no self-consistent connection between them. Some studies included a few atomic layers [39] of the bulk SC in the interface calculation, but the electrostatic potential and the electric field over these layers are far from the values in the bulk. Such calculations can provide, in principle, the value of the Schottky barrier height (SBH). However, they do not provide a self-consistent first-principles description of the electrostatic potential profile of the Schottky barrier. Specifically, none of the first-principles calculations can obtain the barrier thickness.

Many empirical models for the Schottky barrier [3,5,40–44] were developed to solve the Poisson equation with the help of experimental parameters. Several models were developed to connect empirical models with DFT calculations, including, for example, models for solving the Poisson equation for the electrostatic potential [19,45] and models using current-voltage characteristics [46]. With the help of these models, it is possible to find the charge separation at the interface and the value of the SBH. However, these models require empirical parameters derived from experiment, and in these models, the electrostatic potential due to Schottky contact is not included self-consistently into DFT calculations. Moreover, different experimental techniques for Schottky barrier study, for example, based on *I-V* (*C-V*) curves [13,47–49] or by infrared photoresponse measurements, give different results [50]. Inhomogeneous barriers of Schottky contacts also play an important role in the experimental finding of the SBH [44]. All these effects give ambigu-

045429-1

ousness in experimental determination of Schottky contact parameters.

In this paper, we present a DFT approach that enables the simultaneous calculations of all atomic layers from the interface to the bulk SC over the distance of the entire Schottky barrier for arbitrary barrier thickness (Schottky barrier width). The DFT calculations account for the shift in the electrostatic potential as a function of the distance to the interface as well as the local electric field which differ from layer to layer as a function of the distance from the surface. The electrostatic potential and the local electric field are solved from the Poisson equation for the entire semi-infinite system. Both the height and the thickness of the Schottky barrier, along with the charge redistribution over the entire semi-infinite system are obtained as the results of the self-consistent calculation.

The rest of the paper is organized as the following. In the Theory section we start from the Poisson equation and its boundary conditions. This is followed by a description of the metal-induced gap states (MIGS) in the SC and the induced charges due to MIGS. The self-consistent procedure for calculating the electrostatic potential from the DFT is also presented. In the Computational Approach section, we present details of calculations. In the Result section, we present the results of the Si/Al heterostructure, as well as the GaAs-graphene system.

## II. THEORY

### A. Electrostatic potential from induced charges

The charge separation on Schottky contact creates an additional global electrostatic potential, which must be added to the electrostatic potential due to local electrons and nuclei calculated from the DFT. The Poisson equation for the entire system is

$$\nabla^2 \tilde{V}(\mathbf{r}) = -\frac{\tilde{\rho}(\mathbf{r})}{\varepsilon_0}. \tag{1}$$

The charge density includes electrons and nuclei:

$$\tilde{\rho}(\mathbf{r}) = -e \sum_j |\psi_j(\mathbf{r} - \mathbf{R}_j)|^2 + e \sum_j Z_j \delta(\mathbf{r} - \mathbf{R}_j), \tag{2}$$

where $\mathbf{R}_j$ and $Z_j$ are positions and charges of the nuclei. Away from the interface region, the electronic structure is almost bulklike but has small and gradual variations that integrate to form the Schottky potential. To calculate such variations self-consistently, we discretize the Schottky barrier region into several layers. Within each layer, we separate the electrostatic potential into a part that is directly calculated from DFT for a bulk system that is a periodic repetition of the current layer and a second part, which we call the Schottky potential and denote as $V(\mathbf{r})$, that accounts for all the excess charge responsible for the Schottky barrier. The first part is the electrostatic potential of a neutral system. The DFT calculation can include a local electric field (see below) but does not include any excess charge due to doping or MIGS.

The calculation of the Schottky potential $V(\mathbf{r})$ can be greatly simplified if we note that, away from the charge source, the Poisson equation is
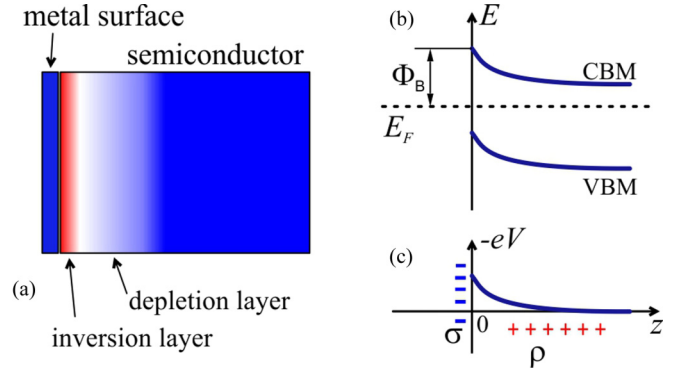
$$\nabla^2 V = 0.$$



FIG. 1. Schottky contact between metal and *n*-type SC. (a) The charge redistribution in the bulk of *n*-type SC (blue represents negative charge and red positive). (b) Band bending in SC. (c) Potential energy of electron in Schottky potential for $\sigma < 0$. $\Phi_B$ shows the SBH. $\sigma$ is the surface charge on the metal surface, and $\rho(z)$ is the charge distribution in the SC bulk creating the excess electrostatic potential $V(z)$. Migration of mobile electrons in *n*-type SC into the metal surface creates the depletion layer near the SC surface. Due to band bending, thermally activated holes create the inversion layer.

The general solution within a layer-periodic geometry is

$$V(\mathbf{r}) = \sum_{mn} V_{mn} \exp[i(mk_x x + nk_y y)] f_{mn}(z),$$

$$f_{mn}(z) = \begin{cases} z, & m = n = 0 \\ \exp\left(-\sqrt{m^2 k_x^2 + n^2 k_y^2}\, z\right) & m \neq 0, \quad n \neq 0, \end{cases}$$

where $k_x$ and $k_y$ are the two-dimensional (2D) reciprocal lattice vectors for a square lattice (generalization to nonsquare lattices is straightforward). The part of the potential that oscillates in the $xy$ plane decays exponentially in the $z$ direction over the distance of the lattice constant. If we neglect the small oscillatory contribution from the excess charge within the current layer, we can consider the Schottky potential to be constant in $x$, $y$ within the layer, and varying only in the $z$ direction (see Fig. 1).

The gradient of Schottky potential creates an electric field which acts on each layer that in turn induces an additional dipole response from the SC. The Schottky potential, which should be added to every cell of DFT calculations, can be found by solving the Poisson equation:

$$\nabla^2 V(z) = -\frac{\rho(z)}{\varepsilon_0} + \frac{\nabla \cdot \mathbf{P}(z)}{\varepsilon_0}, \tag{3}$$

where $\rho(z)$ is the density of induced charges in the SC due to doping, thermal holes and electrons, and MIGS (see Sec. II B). The term $-(\nabla \cdot \mathbf{P})$ is the charge density due to the polarization $\mathbf{P}$ of the media due to local electric field arising from the Schottky potential.

We set the potential at $z \to +\infty$ to zero (see Fig. 1):

$$V(z)|_{z \to +\infty} = 0, \tag{4}$$

and the boundary condition at the surface corresponds to

$$\frac{\partial V}{\partial z}(0) = -\frac{\sigma}{\varepsilon_0} + \frac{P(0)}{\varepsilon_0}, \qquad (5)$$

where $\sigma$ is the surface charge density accumulated at the contact surface and $P(0)$ is the polarization of the SC at the surface.

The electrostatic potential due to charge $\rho(z)$ in the bulk and the charge at the metal surface can be calculated as the potential from the charged planes $\rho dz'$ and $\sigma$:

$$V_\rho(z) = -\frac{1}{2\varepsilon_0}\int_0^{+\infty}\rho(z')|z-z'|dz' - \frac{1}{2\varepsilon_0}\sigma|z|, \quad (6)$$

where $\varepsilon_0$ is the vacuum dielectric constant. Here, $\sigma$ is equal to the total charge in the bulk SC with opposite sign:

$$\sigma = -\int_0^{+\infty}\rho(z')dz', \qquad (7)$$

to ensure total charge neutrality of the system. The first-principles approach to calculate the excess charge density $\rho$ will be described in Subsec. B. The expression in Eq. (6) can be simplified by considering the charge neutrality condition in Eq. (7) and setting the potential at $z \to +\infty$ to zero according to the boundary condition in Eq. (4):

$$V_\rho(z) = -\frac{1}{\varepsilon_0}\int_z^{+\infty}\rho(z')(z'-z)dz'. \qquad (8)$$

The electric field due to the charge redistribution induces the dipole moment of the media (polarization **P**) which creates, in turn, the electric field with opposite direction. These induced dipole moments create an additional contribution to the electrostatic potential:

$$V_P(z) = \frac{1}{2\varepsilon_0}\int_0^{+\infty}P(z')\text{sign}(z-z')dz', \qquad (9)$$

where $P(z)$ is the polarization of the bulk SC in the direction of the field. Using the same procedure as with the derivation of Eq. (8), we can rewrite Eq. (9) in the following form:

$$V_P(z) = -\frac{1}{\varepsilon_0}\int_z^{+\infty}P(z')dz'. \qquad (10)$$

The total excess electrostatic potential is the sum of the two contributions in Eqs. (8) and (10):

$$V(z) = V_\rho(z) + V_P(z). \qquad (11)$$

The electrostatic potential in Eq. (11) has two impacts on the Schottky contact. First, it shifts the energy of the electronic states for each layer of the bulk SC by the potential energy $-eV(z)$, and second, the gradient of the potential $V$ defines the local electric field acting on the current layer of the SC. Previous attempts of first-principles methods for calculating the Schottky barrier based on DFT [10–19] do not include the Schottky potential in the DFT self-consistency cycle due to a very wide depletion layer ($\sim$100–1000 Å for high doping concentration), yielding band structure of the SC without the effect of the local electric field due to the Schottky contact.

### B. Induced charge distribution due to band bending

Bringing a SC into contact with a metal over a clean interface accumulates or depletes free mobile charges from the SC, depending on the difference in the electrostatic potential on two sides of the interface. This redistribution of the charges creates a volume charge density $\rho(z)$ in the SC region next to the interface and a surface charge density $\sigma$ on the metal side, keeping the total charge of the system equal to zero. The charge distribution near an interface on the SC side usually contains two main contributions. One is from the so-called MIGS [51] or, in the case of a surface, surface-induced gap states (SIGS); the other is from free carriers, including both holes and electrons in the SC due to doping or thermal activation. The total excess charge density is the sum of the contributions from holes, electrons, MIGS, and the charged dopants that act as a compensating background charge in the bulk:

$$\rho(z) = \rho_h(z) + \rho_e(z) + \rho_{\text{MIGS}}(z) + \rho_d, \qquad (12)$$

where the dopant charge is equal to $\rho_d = -[\rho_h(z) + \rho_e(z)]|_{z\to+\infty}$ and depends on the Fermi level position.

The charge distribution of the holes in the valence band is calculated according to the Fermi-Dirac distribution and increases (or decreases) closer to the interface due to the bending of the valence band by the electrostatic energy $-eV(z)$, where $V(z)$ is the electrostatic potential due to the induced excess charge given by Eq. (11). To account for this extra charge, the DOS of each layer of the bulk SC is calculated under the influence of the electric field $E = -\nabla V(z)$. To obtain the induced charge, integration over the energy up to valence band maximum (VBM) $E_{\text{VBM}} - eV(z)$ is equivalent to the shifting of the Fermi level down by $-eV(z)$:

$$\rho_h(z) = \frac{e}{\Omega}\int_{-\infty}^{E_{\text{VBM}}-eV(z)}[1-f(E)]D_b\{E-[-eV(z)]\}dE, \qquad (13)$$

where $\Omega$ is the volume of the cell, $f(E)$ is the Fermi-Dirac function, and $D_b(E)$ is the DOS of the SC bands, modified by the local electric field due to the induced charge density.

The electron carrier contribution to the excess charge distribution is calculated by a similar integration of the DOS from the conduction band minimum (CBM) up to $+\infty$:

$$\rho_e(z) = -\frac{e}{\Omega}\int_{E_{\text{CBM}}-eV(z)}^{+\infty}f(E)D_b\{E-[-eV(z)]\}dE. \quad (14)$$

Another contribution from the electron density is from the MIGS or SIGS, which are the evanescent states within the band gap [3,5,51–57] and form on the surface of the SC and penetrate into the bulk, generating a charge distribution. A powerful tool for calculating the MIGS from first-principles is the framework of complex band structure (CBS) [54,58–60] in the SC. This method has been used, for example, for calculation of carrier mobility in heterojunctions [61,62] and tunneling coefficients in strongly-correlated systems [63].

The wave functions of the Bloch electrons in the metal have exponential tails extending into the SC and manifest as the evanescent states. These evanescent states are described by the CBS [59,60] and are energy dependent. We express the
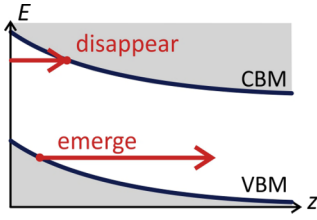
FIG. 2. Emergence and disappearance of MIGS near the bended VBM and CBM at the gap of semiconductor which was exposed to the electron wave functions in the metal according to Eq. (16).

evanescent state wave functions in the form

$$\Psi(z) \sim \chi(\mathbf{k}) \exp\left[-\kappa_z(E, \mathbf{k})z\right], \tag{15}$$

where $\chi(\mathbf{k})$ is a periodic function in the plane perpendicular to $z$, $\kappa_z$ is the penetration (decay) rate, and the DOS of MIGS is defined by the expression in Eq. (16). It is necessary to consider that, due to Schottky contact, each layer of the bulk SC exhibits the influence of local electric field due to Schottky potential, and thus, the CBS can be different from layer to layer of the SC.

The MIGS contribution is proportional to the exponential factor of the CBS decay rate $\kappa_z(E, \mathbf{k})$:

$$
\begin{aligned}
&\rho_{\text{MIGS}}(z) \\
&= -\frac{e}{\Omega} \int_{E_{\text{VBM}} - eV(z)}^{E_{\text{CBM}} - eV(z)} f(E) D_{\text{MIGS}}\{\sigma, E - [-eV(z)], z\} dE,
\end{aligned}
\tag{16}
$$

where

$$
\begin{aligned}
D_{\text{MIGS}}(\sigma, E, z) = \int d\mathbf{k} \Big\{ & D_i^L(\sigma, E, \mathbf{k}) \exp\left[-2\kappa_z^L(E, \mathbf{k})z\right] \\
& + D_i^H(\sigma, E, \mathbf{k}) \exp\left[-2\kappa_z^H(E, \mathbf{k})z\right] \Big\},
\end{aligned}
\tag{17}
$$

is the DOS of a MIGS. Here, $D_i^{L/H}(\sigma, E, \mathbf{k})$ are the contributions to the projected DOS (PDOS) of the interfacial layer for light and heavy holes, correspondingly, and $\kappa_z^{L/H}(E, \mathbf{k})$ are the decaying rates for light and heavy holes. In Eq. (17), we also consider that the DOS is proportional to the square of the wave function in Eq. (15).

The SC energy gap near the surface is shifted due to the Schottky potential; therefore, the MIGS emerge and disappear near the bended VBM and CBM (see Fig. 2). These states are considered by matching boundary conditions for $D_i^{L/H}(\sigma, E, \mathbf{k})$ at each position $z$.

The energy shift $\Delta E$ of the surface states due to migrated electrons to the surface (see Fig. 3) is determined by the surface charge density:

$$\sigma = -\frac{e}{S} \int_{E_F - \Delta E}^{E_F} f(E) D_0\{E - [-eV(0)]\} dE, \tag{18}$$

where $(E_F - \Delta E)$ is the Fermi level of the neutral interface, $D_0(E)$ is the PDOS of the surface interface, which includes the metal surface and the surface layer of the SC, and $S$ is the surface area of the cell.
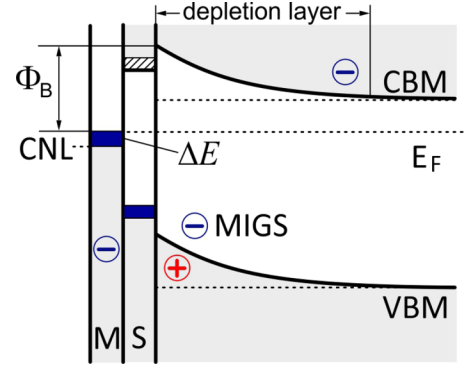


FIG. 3. Scheme for *n*-type doped SC in contact with metal surface (M), blue area $\Delta E$ shows energy filling level due to migrated electrons from SC, minus sign on metal surface shows migrated electrons from SC, minus sign in the gap of SC shows MIGS, and plus sign near the bended VBM shows thermally activated holes responsible for creation of inversion layer. CNL is a charge neutrality level corresponding to zero charge on the interface. On the SC surface (S), it is shown two areas corresponding to the surface states; dashed area is unfilled, and blue area is filled surface states. $\Phi_B$ shows the SBH.

### C. Self-consistent solution for Schottky contact

The effect of the electrostatic potential due to the Schottky contact can be added to the DFT calculations by introducing an equivalent electric field $\mathbf{E} = -\nabla V(z)$ which differs from layer to layer in the bulk SC, in addition to the local shift of the Fermi energy relative to the band structure. The induced charge density due to the contact is calculated from the local electrostatic potential in Eq. (11), and induced polarization due to electric field $\mathbf{E} = -\nabla V(z)$ is calculated in DFT. On the other hand, the overall shift in the electrostatic potential due to the Schottky contact is defined by the induced charge in Eq. (12). Then the Schottky potential is defined as self-consistent equilibrium among $V$, $\rho$, $\mathbf{E}$, $P$, and the charge on the interface $\sigma$:

$$V\{\rho[V(z)], P(z), \mathbf{E}, \sigma\} \equiv V(z). \tag{19}$$

To find the equilibrium in Eq. (19), we use a self-consistent procedure. A good approximate initial charge distribution is

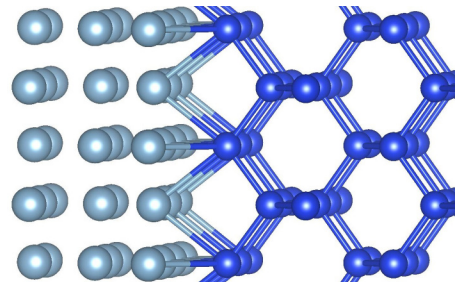$$\rho(z) = \rho_0 \exp\left(-\frac{z}{z_0}\right). \tag{20}$$



FIG. 4. Al(100)-Si(100) heterostructure. Al atoms in light blue and Si atoms in blue. In the contact layer, Si-Al bonds are created.

TABLE I. Schottky barrier height (SBH), potential energy ($-eV$), energy shift $\Delta E$, depletion layer width (DLW), inversion layer width (ILW), surface charge density ($\sigma$), and electric field (E) at the surface as functions of electron doping concentration ($\rho_n$) for Si-Al system for $T = 300$ K.

| $E_F - E_{VBM}$ (eV) | $\rho_n$ (cm$^{-3}$) | SBH (eV) | $-eV$ (eV) | $\Delta E$ (eV) | DLW (Å) | ILW (Å) | $\sigma$ (cm$^{-2}$) | E (V/Å) |
|---|---|---|---|---|---|---|---|---|
| 0.78 | $-4.02 \times 10^{13}$ | 0.590 | 0.250 | $4.50 \times 10^{-5}$ | 27 892 | 1001 | $-1.05 \times 10^{10}$ | $-1.59 \times 10^{-5}$ |
| 0.89 | $-2.72 \times 10^{15}$ | 0.590 | 0.360 | $4.63 \times 10^{-4}$ | 4031 | 87.4 | $-1.08 \times 10^{11}$ | $-1.64 \times 10^{-4}$ |
| 0.93 | $-1.28 \times 10^{16}$ | 0.589 | 0.365 | $1.06 \times 10^{-3}$ | 1971 | 37.4 | $-2.47 \times 10^{11}$ | $-3.75 \times 10^{-4}$ |
| 1.00 | $-1.99 \times 10^{17}$ | 0.586 | 0.466 | $4.33 \times 10^{-3}$ | 553.3 | 8.5 | $-1.04 \times 10^{12}$ | $-1.58 \times 10^{-3}$ |
| 1.12 | $-1.72 \times 10^{19}$ | 0.555 | 0.555 | $3.57 \times 10^{-2}$ | 66.8 | 0.81 | $-1.09 \times 10^{13}$ | $-1.66 \times 10^{-2}$ |

The corresponding charge accumulated at the contact surface due to Eq. (20) is

$$\sigma = -\rho_0 z_0. \quad (21)$$

The electrostatic potential from charge distribution in Eq. (20) according to Eq. (8) is

$$V(z) = V_0 \exp\left(-\frac{z}{z_0}\right), \quad (22)$$

where $V_0 = \rho_0 z_0^2 / \varepsilon_0$, $\rho_0$ and $z_0$ are taken from the experimental data [64,65], which yield starting estimates $z_0 \approx 1000$ Å and $-eV(0) = 0.5$ eV. Using Eq. (20) as the initial guess, we calculate the charge distribution in Eq. (12) across the entire barrier region and then calculate the new potential in Eq. (8) corresponding to the new charge distribution, the electric field as the gradient of $V(z)$, and the corresponding potential due to the polarization in Eq. (10). We then repeat the whole procedure until convergence [reaching self-consistency in Eq. (19) among $V(z)$, $\rho(z)$, E($z$), and $P(z)$]. The self-consistency between the charge redistribution and the electrostatic potential determines the Schottky barrier, including both its height and thickness [depletion (DLW) and inversion layer widths (ILW)].

## III. COMPUTATIONAL APPROACH

### A. Technical details

The calculations were carried out using DFT with the Perdew-Burke-Ernzerhof exchange-correlation functional [66] and the projector augmented wave method [67,68], implemented in the QUANTUM ESPRESSO package [69]. For the relaxation of the structures, we used the Vienna *Ab initio* Simulation Package (VASP) [70,71] and generalized gradient approximation with the optB88 exchange-correlation functional including the van der Waals correction [72–74] to account for the interaction of graphene (Gr) with the surface of GaAs. An energy cutoff of 500 eV was used for the plane-wave expansion. The DOS of GaAs crystal was calculated for the primitive cell consisting of two atoms with $31 \times 31 \times 31$ **k**-mesh. The interface system was represented by a Gr layer in contact with GaAs(111) surface, which consisted of a surface layer and five additional layers of GaAs bulk. For the surface layer, we used surface reconstruction ($2 \times 2$) with a vacancy of Ga, which is described in detail in Sec. IV C. The last layer of GaAs was terminated by H.75 pseudo-hydrogen atoms to fill all dangling bonds with the electrons from hydrogen atoms. The interface calculation for the GaAs-Gr system was taken for $15 \times 15$ **k**-mesh, which corresponds to the total of 27 **k**-points. The CBS calculations were performed in a cell consisting of three atoms of Ga and three atoms of As, which formed three layers of GaAs, to simulate the decaying process in the direction perpendicular to the (111) surface. The **k**-mesh of the cell was set to $15 \times 15 \times 15$, and the CBS decaying rates were calculated for 27 **k**-points corresponding to the interface calculations to calculate the MIGS density in Eq. (17).

The Si-Al heterostructure was created by contacting the Si(100) surface with the Al(100) surface in a such a way that Al atoms were placed against the hollow positions on the Si(100) surface (Fig. 4). The cell consisted of 12 Si atoms, six Al atoms, and one hydrogen, which terminated the opposite surface of Si. The lattice parameter of Si crystal was set to 5.430 Å, and Al atoms on the surface (100) were connected to corresponding hollow positions on the Si surface. The lattice parameter of Al was decreased from 4.095 to 3.840 Å to match the Si atom positions, which created the strain of 6.6% in the Al layer. One layer of Si and all Al atoms were allowed to relax in the $z$ direction. The Al-Si contact created chemical bonds between Si and Al atoms. The Si-Si bond length in the contact layer was increased from 2.351 to 2.399 Å due to new chemical bonds with Al atoms, and the Al-Al bond length was increased from 2.706 Å in the compressed Al layer to 2.853 Å in the Al-Si contact layer. The relaxed bond length of Si-Al

TABLE II. Schottky barrier height (SBH), potential energy ($-eV$), energy shift $\Delta E$, depletion layer width (DLW), inversion layer width (ILW), surface charge density ($\sigma$), and electric field (E) at the surface as functions of hole doping concentration ($\rho_p$) for Si-Al system for $T = 300$ K.

| $E_F - E_{VBM}$ (eV) | $\rho_p$ (cm$^{-3}$) | SBH (eV) | $-eV$ (eV) | $\Delta E$ (eV) | DLW (Å) | ILW (Å) | $\sigma$ (cm$^{-2}$) | E (V/Å) |
|---|---|---|---|---|---|---|---|---|
| 0.37 | $1.70 \times 10^{13}$ | 0.529 | $-0.159$ | $-4.37 \times 10^{-4}$ | 33 655 | 2287 | $1.01 \times 10^{11}$ | $1.19 \times 10^{-4}$ |
| 0.25 | $1.76 \times 10^{15}$ | 0.528 | $-0.278$ | $-1.52 \times 10^{-3}$ | 4494 | 125.1 | $3.56 \times 10^{11}$ | $4.42 \times 10^{-4}$ |
| 0.12 | $2.68 \times 10^{17}$ | 0.523 | $-0.403$ | $-6.88 \times 10^{-3}$ | 443.9 | 8.2 | $1.69 \times 10^{12}$ | $2.38 \times 10^{-3}$ |
| 0.00 | $2.21 \times 10^{19}$ | 0.490 | $-0.490$ | $-4.01 \times 10^{-2}$ | 55.5 | 0.76 | $1.25 \times 10^{13}$ | $1.87 \times 10^{-2}$ |

TABLE III. Schottky barrier height (SBH), potential energy ($-eV$), energy shift $\Delta E$, depletion layer width (DLW), inversion layer width (ILW), surface charge density ($\sigma$), and electric field (E) at the surface as functions of electron concentration ($\rho_n$) for GaAs-Gr system for $T = 300$ K.

| $E_{\mathrm{F}}$-$E_{\mathrm{VBM}}$ (eV) | $\rho_n$(cm$^{-3}$) | SBH (eV) | $-eV$ (eV) | $\Delta E$ (eV) | DLW (Å) | ILW (Å) | $\sigma$(cm$^{-2}$) | E (V/Å) |
|---|---|---|---|---|---|---|---|---|
| 1.19 | $-2.00 \times 10^{13}$ | 0.738 | 0.508 | $3.43 \times 10^{-5}$ | 63 770 | 884 | $-1.21 \times 10^{10}$ | $-1.49 \times 10^{-5}$ |
| 1.31 | $-2.07 \times 10^{15}$ | 0.738 | 0.628 | $3.82 \times 10^{-4}$ | 6995 | 74.0 | $-1.37 \times 10^{11}$ | $-1.70 \times 10^{-4}$ |
| 1.40 | $-5.94 \times 10^{16}$ | 0.736 | 0.716 | $2.16 \times 10^{-3}$ | 1395 | 12.8 | $-7.89 \times 10^{11}$ | $-9.75 \times 10^{-4}$ |
| 1.42 | $-1.15 \times 10^{17}$ | 0.735 | 0.735 | $3.01 \times 10^{-3}$ | 1014 | 9.2 | $-1.11 \times 10^{12}$ | $-1.37 \times 10^{-3}$ |

was 2.629 Å. The DOS of the Si crystal was calculated for the primitive cell consisting of two atoms, and the **k**-mesh was set to $51 \times 51 \times 51$. The interface calculation for the Al-Si system was taken for $21 \times 21$ **k**-mesh, which corresponds to the total of 121 **k**-points. The CBS calculations were performed in an eight-atom conventional cell of Si crystal to simulate the decaying process in the direction perpendicular to the (100) surface. The **k**-mesh of the eight-atom cell was set to $15 \times 15 \times 15$, and the CBS decaying rates were calculated for 121 **k**-points corresponding to the interface calculation.

## B. Self-consistent procedure

The self-consistent procedure consists of three independent sets of DFT calculations:

(1) DFT calculation of the primitive cell of GaAs for different values of the electric field corresponding to each layer of the SC, to get the DOS $D_b(E)$ of the SC bands, used in Eqs. (13) and (14), and the induced dipole moments of each layer under the local electric field. To get the band gap of GaAs in accordance with the experimental value of 1.42 eV, we applied the scissor correction [75,76].

(2) Calculation of the CBS of the GaAs(111) slab surface containing three GaAs layers to get the decay rate $\kappa_z$ needed in Eq. (17).

(3) Calculation of the PDOS $D_i(E, \mathbf{k})$ of the interfacial layer in the Gr-GaAs(111) system. The bottom layer of the Gr-GaAs(111) system is terminated with hydrogen and is not included in the PDOS. PDOS $D_i(E, \mathbf{k})$ is used to separate light and heavy hole contribution (see Sec. D) and to calculate MIGS density according to Eq. (17).

These DFT calculations are stitched together in the self-consistent procedure by the following additional steps, starting from the initial approximation to the potential $V(z)$ in Eq. (22) and calculating

(1) the electron and hole charge densities in each layer of the SC in Eqs. (13) and (14) as functions of $z$ using $D_b[E]$, updated from DFT and $V(z)$;

(2) the induced charge density due to MIGS using $D_i(E, \mathbf{k})$, updated from DFT, $V(z)$, and $\kappa_z$ also updated from DFT;

(3) the total charge density $\rho(z)$ in Eq. (12);

(4) the new potential $V(z)$ in Eqs. (6) and (8) from the total induced charge density $\rho(z)$ and the local electric field E(z), which is used in the DFT calculations of the next iteration;

(5) the compensating surface charge density $\sigma$ in Eq. (7) and the energy shift of the surface states $\Delta E$ defined in Eq. (18).

Steps 2–5 are repeated until consistency between $\rho(z)$ and $V(z)$ is reached.

## C. Integration over k-space

The DOS of the interface at the gap of the SC has a Gaussian-like distribution at $\Gamma$ with a finite width. The CBS decay rate $\kappa_z(E, \mathbf{k})$ has the slowest decaying rates at the $\Gamma$ point. Because of that, at large distances, the interfacial DOS $D_i(\sigma, E, \mathbf{k}) \exp[-2\kappa_z(E, \mathbf{k})z]$ has a sharp peak at $\Gamma$, and the numerical integration in Eq. (17) over $d\mathbf{k}$ is inaccurate and produces overestimated values. To improve the accuracy of the integration for large distances, we use parabolic approximation for the CBS, and write the DOS as a Gaussian distribution over $\mathbf{k}$:

$$D_i(E, \mathbf{k}, z) \approx D_i(E, 0, z) \exp\left[-\frac{k_r^2}{\kappa_z(E, 0)}z\right], \quad (23)$$

where $k_r^2 = k_x^2 + k_y^2$. This allows us to calculate the integral in Eq. (17) over the Brillouin zone analytically and connect to the numerical solution at small $z$ by matching the corresponding width of the Gaussian and numerical distributions. The detailed derivation of the integration scheme and the

TABLE IV. Schottky barrier height (SBH), potential energy ($-eV$), energy shift $\Delta E$, depletion layer width (DLW), inversion layer width (ILW), surface charge density ($\sigma$), and electric field (E) at the surface as functions of hole concentration ($\rho_p$) for GaAs-Gr system for $T = 300$ K.

| $E_{\mathrm{F}}$-$E_{\mathrm{VBM}}$ (eV) | $\rho_p$ (cm$^{-3}$) | SBH (eV) | $-eV$ (eV) | $\Delta E$ (eV) | DLW (Å) | ILW (Å) | $\sigma$(cm$^{-2}$) | E (V/Å) |
|---|---|---|---|---|---|---|---|---|
| 0.32 | $1.05 \times 10^{14}$ | 0.680 | $-0.360$ | $-1.19 \times 10^{-3}$ | 23 270 | 494.5 | $4.32 \times 10^{11}$ | $4.41 \times 10^{-4}$ |
| 0.26 | $1.07 \times 10^{15}$ | 0.680 | $-0.420$ | $-1.60 \times 10^{-3}$ | 7879 | 136.8 | $5.82 \times 10^{11}$ | $6.07 \times 10^{-4}$ |
| 0.20 | $1.09 \times 10^{16}$ | 0.679 | $-0.479$ | $-2.36 \times 10^{-3}$ | 2646 | 39.3 | $8.65 \times 10^{11}$ | $9.38 \times 10^{-4}$ |
| 0.14 | $1.11 \times 10^{17}$ | 0.677 | $-0.537$ | $-4.29 \times 10^{-3}$ | 880.2 | 11.3 | $1.60 \times 10^{12}$ | $1.83 \times 10^{-3}$ |
| 0.08 | $1.12 \times 10^{18}$ | 0.672 | $-0.592$ | $-9.80 \times 10^{-3}$ | 293.3 | 3.3 | $3.84 \times 10^{12}$ | $4.58 \times 10^{-3}$ |
| 0.00 | $2.00 \times 10^{19}$ | 0.650 | $-0.650$ | $-3.20 \times 10^{-2}$ | 73.6 | 0.73 | $1.48 \times 10^{13}$ | $1.81 \times 10^{-2}$ |

TABLE V. Schottky barrier height (SBH), potential energy ($-eV$), energy shift $\Delta E$, depletion layer width (DLW), inversion layer width (ILW), surface charge density ($\sigma$), and electric field (E) at the surface as functions of the temperature for electron doping corresponding to Fermi level at CBM for GaAs-Gr system.

| $T$ (K) | $\rho_n$ (cm$^{-3}$) | SBH (eV) | $-eV$ (eV) | $\Delta E$ (eV) | DLW (Å) | ILW (Å) | $\sigma$ (cm$^{-2}$) | E (V/Å) |
|---|---|---|---|---|---|---|---|---|
| 150 | $-3.72 \times 10^{16}$ | 0.737 | 0.737 | $1.73 \times 10^{-3}$ | 1797 | – | $-6.42 \times 10^{11}$ | $-7.93 \times 10^{-4}$ |
| 200 | $-5.89 \times 10^{16}$ | 0.736 | 0.736 | $2.18 \times 10^{-3}$ | 1421 | 7.7 | $-8.04 \times 10^{11}$ | $-9.93 \times 10^{-4}$ |
| 250 | $-8.46 \times 10^{16}$ | 0.736 | 0.736 | $2.60 \times 10^{-3}$ | 1188 | 8.5 | $-9.59 \times 10^{11}$ | $-1.18 \times 10^{-3}$ |
| 300 | $-1.15 \times 10^{17}$ | 0.735 | 0.735 | $3.01 \times 10^{-3}$ | 1014 | 9.2 | $-1.11 \times 10^{12}$ | $-1.37 \times 10^{-3}$ |
| 350 | $-1.49 \times 10^{17}$ | 0.735 | 0.735 | $3.42 \times 10^{-3}$ | 889.9 | 9.8 | $-1.26 \times 10^{12}$ | $-1.56 \times 10^{-3}$ |

method to connect the numerical and analytical solutions are described in the Appendix.

### D. Light and heavy hole separation in PDOS

The PDOS of the interfacial layer contains the contributions from heavy and light holes, which have different decaying rates $\kappa_z(E, \mathbf{k})$. The interfacial layer selected for the PDOS should be far enough from the surface layer not to include the surface states, which significantly differ from the bulk states. This layer also should be far enough from the bottom layer of the interface calculation not to include the hydrogen states. From six layers of the system for the interface calculation, we are taking the PDOS for the third and fourth layers and writing the expressions

$$D_i^3(E, \mathbf{k}) = D_i^L(E, \mathbf{k}) \exp\left[-2\kappa_z^L(E, \mathbf{k})z_3\right]$$
$$+ D_i^H(E, \mathbf{k}) \exp\left[-2\kappa_z^H(E, \mathbf{k})z_3\right]\}, \quad (24)$$

$$D_i^4(E, \mathbf{k}) = D_i^L(E, \mathbf{k}) \exp\left[-2\kappa_z^L(E, \mathbf{k})z_4\right]$$
$$+ D_i^H(E, \mathbf{k}) \exp\left[-2\kappa_z^H(E, \mathbf{k})z_4\right]\}, \quad (25)$$

where $D_i^{3/4}(E, \mathbf{k})$ are the PDOS calculated for the third and fourth layers, and $z_{3/4}$ are the positions of the third and fourth layers. Knowing the decaying rates for light and heavy holes, we can solve the set of Eqs. (24) and (25) for $D_i^L(E, \mathbf{k})$ and $D_i^H(E, \mathbf{k})$ for each point ($E$,$\mathbf{k}$) and separate the light hole contribution to the PDOS from heavy holes to use with the corresponding decay rates.

### IV. RESULTS

We now apply our method on a heterostructure of a Si(100) surface in contact with a Al(100) surface and 2D semimetal in contact with a SC [77] as a GaAs-Gr heterostructure. These

two heterostructures have different connection types between metal and SC. For the GaAs-Gr system, the connection is due to Van der Waals forces, whereas the Si/Al system creates chemical bonds between metal and SC atoms.

The Schottky contact parameters, SBH, Schottky potential energy, DLW, ILW, surface charge density, and electric field at the surface, depending on doping concentration are summarized at Tables I and II for the Si/Al heterostructure and Tables III and IV for the GaAs-Gr system. Tables V and VI show the dependence of Schottky parameters on temperature. We define the DLW for a $p$ ($n$)-type doped SC as a region where the main carrier concentration $\rho_p$ ($\rho_n$) together with the background charge $\rho_d$ is reduced by $e$ from the value at the surface (see Figs. 5 and 6). Correspondingly, we define the ILW for a $p$ ($n$)-type doped SC as a region where the thermally activated minority $n$ ($p$)-type carrier concentration is reduced by $e$ from the value at the surface. We should point out here that extracting the width of the depletion layer from the linear dependence of the electric field due to the Schottky potential gives a close result for DLW obtained from our definition. Thus, for the GaAs-Gr system for $n$-type doping of $1.15 \times 10^{17}$ cm$^{-3}$, the DLW calculated from the linear dependence of the electric field gives 971 Å, whereas from our method, it is 1014 Å.

### A. Schottky contact Al(100)-Si(100)

Tables I and II show the results of self-consistent solutions for SBH, DLW, ILW, total charge accumulated at the metal surface, and electric field close to the SC surface for the system for $n$- and $p$-type doping, correspondingly. The space distributions for the electrons and holes for depletion and inversion layers are presented in Figs. 5 and 6.

There are many experimental studies on Al-Si contacts using $C$-$V$, $I$-$V$, and photoelectric measurements [78–83] for $n$- and $p$-type doped Si. In real experiments, the surface of Si
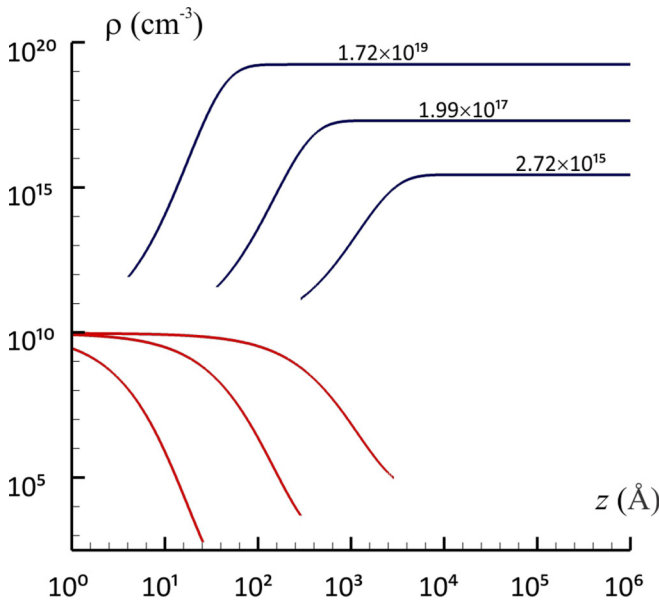
TABLE VI. Schottky barrier height (SBH), potential energy ($-eV$), energy shift $\Delta E$, depletion layer width (DLW), inversion layer width (ILW), surface charge density ($\sigma$), and electric field (E) at the surface as functions of the temperature for hole doping corresponding to Fermi level at VBM for GaAs-Gr system.

| $T$ (K) | $\rho_p$ (cm$^{-3}$) | SBH (eV) | $-eV$ (eV) | $\Delta E$ (eV) | DLW (Å) | ILW (Å) | $\sigma$ (cm$^{-2}$) | E (V/Å) |
|---|---|---|---|---|---|---|---|---|
| 150 | $5.81 \times 10^{18}$ | 0.664 | $-0.664$ | $-1.79 \times 10^{-2}$ | 137.8 | – | $8.49 \times 10^{12}$ | $1.03 \times 10^{-2}$ |
| 200 | $9.82 \times 10^{18}$ | 0.659 | $-0.659$ | $-2.28 \times 10^{-2}$ | 105.8 | 0.62 | $1.07 \times 10^{13}$ | $1.30 \times 10^{-2}$ |
| 250 | $1.46 \times 10^{19}$ | 0.654 | $-0.654$ | $-2.75 \times 10^{-2}$ | 86.6 | 0.68 | $1.28 \times 10^{13}$ | $1.56 \times 10^{-2}$ |
| 300 | $2.00 \times 10^{19}$ | 0.650 | $-0.650$ | $-3.20 \times 10^{-2}$ | 73.6 | 0.73 | $1.48 \times 10^{13}$ | $1.81 \times 10^{-2}$ |
| 350 | $2.61 \times 10^{19}$ | 0.645 | $-0.645$ | $-3.63 \times 10^{-2}$ | 64.4 | 0.78 | $1.67 \times 10^{13}$ | $2.05 \times 10^{-2}$ |

FIG. 5. Induced charge density of electrons (absolute value; blue) and holes (red) for Si-Al system for $T = 300\,\mathrm{K}$, $n$-type doping with concentrations $\rho_n = 1.72 \times 10^{19}\,\mathrm{cm^{-3}}$, $1.99 \times 10^{17}\,\mathrm{cm^{-3}}$, and $2.72 \times 10^{15}\,\mathrm{cm^{-3}}$, respectively.

often has an oxide layer, which contains a positive charge and increases the SBH. Card [81] pointed out that the results for the SBH are very sensitive to the condition of the Si surface before Al evaporation. Thus, experimental measurements for the SBH for $n$-type doped Si vary from 0.61 to 0.77 eV and depend on growing condition, treatment procedure for oxide layer, annealing of the surfaces, and even on resting time after the treatment. Pellegrini [84,85] pointed out that, for an
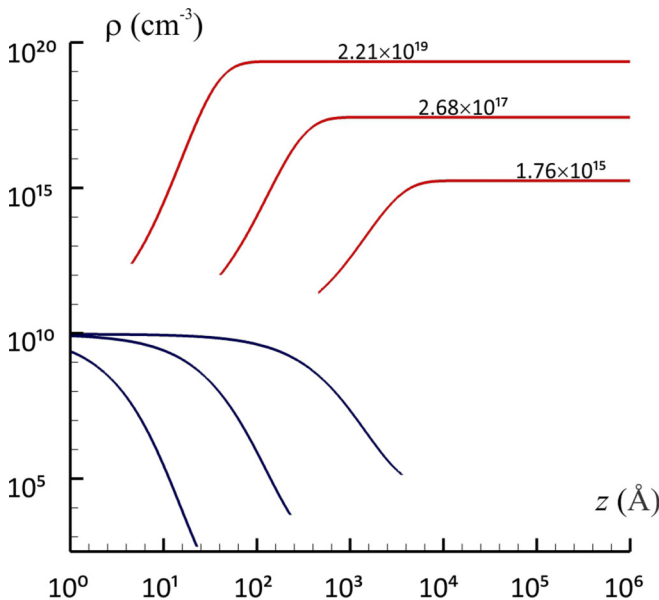


FIG. 6. Induced charge density of holes (red) and electrons (absolute value; blue) for Si-Al system for $T = 300\,\mathrm{K}$, $p$-type doping with concentrations $\rho_p = 2.21 \times 10^{19}\,\mathrm{cm^{-3}}$, $2.68 \times 10^{17}\,\mathrm{cm^{-3}}$, and $1.76 \times 10^{15}\,\mathrm{cm^{-3}}$, respectively.

$n$-type SC, the SBH derived from $C$-$V$ measurements should always be higher (and for $p$-type should always be lower) than those obtained from $I$-$V$ and photoelectric measurements because quantum-mechanical penetration of electrons from the metal into the SC energy gap makes the barrier lower than that deduced from the capacitance measurements. Thanailakis [82] used $I$-$V$ measurements and got the values of 0.61 eV for the SBH for Al-Si contact prepared by Al evaporation on a vacuum-cleaved Si surface. Tejedor *et al.* [42] calculated with Green function formalism [86] the SBH of 0.60 eV for Al-Si contact by including the surface barrier effect using the jellium model and surface (virtual) states using a two-band narrow-gap model [87]. Our result for the SBH obtained self-consistently for $n$-type doped Si is 0.59 eV (see Table I), in good agreement with the experimental result of Thanailakis [82] and calculated result by Tejedor *et al.* [42].

The depletion layer for doping concentration of $1.72 \times 10^{19}\,\mathrm{cm^{-3}}$ is 67 Å, whereas the inversion layer is 0.8 Å. The charge accumulated at the metal surface is $1.09 \times 10^{13}\,\mathrm{cm^{-2}}$, and electric field at the SC surface is $1.66 \times 10^{-2}\,\mathrm{V/Å}$. For doping concentration of $1.99 \times 10^{17}\,\mathrm{cm^{-3}}$ corresponding to one experiment [81], the electric field at the surface is $1.58 \times 10^{-3}\,\mathrm{V/Å}$, which is in good agreement with the experimental value of $10^{-3}\,\mathrm{V/Å}$ [81]. Reducing bulk doping (by tuning the Fermi energy) causes the width of depletion and inversion layers to increase and the charge accumulated at the metal surface to decrease, accompanied by smaller band bending. The smaller charge on the interface results in smaller $\Delta E$ and larger $\Phi_\mathrm{B}$ (see Fig. 3). This trend is consistent with previous empirical calculation by Osvald and Dobrocka [88]. Our results show the SBH of 0.590 eV for low doping concentration and 0.567 eV for higher doping concentration (see Table I). Experimental measurements for DLW for Si contacts under zero bias show values from a fraction of a micrometer to tens of micrometers, depending on doping concentration and the geometry of the contact [89].

The ILW (see Tables I, II, V, and VI) depends on doping concentration. For high doping concentration $\sim 10^{19}\,\mathrm{cm^{-3}}$, the ILW is $<1$ Å, whereas for doping of $\sim 10^{13}\,\mathrm{cm^{-3}}$, the ILW is $>1000$ Å. Many experimental [90–95] and theoretical [90,96,97] works show strong influence of the inversion layer on Schottky parameters of the structures. Experimentally, the inversion layer can be detected for lightly doped SCs only [96]. Empirical models [90,96,97] for describing the inversion layer are based on the assumption that the inversion layer is the interfacial layer of two to three atomic dimensions and even set the ILW to zero in the charge-sheet approximation [98]. Our results show that, for small doping concentration, the ILW may exceed 1000 Å (see Figs. 5 and 6).

### B. CBS of bulk GaAs

Figure 7 shows the CBS of bulk GaAs along the direction perpendicular to (111) calculated by PWCOND software of the QUANTUM ESPRESSO package [69,99]. The main band $\kappa_z$ responsible for the evanescent states in the gap is bolded in red in Fig. 7 and corresponds to light hole contribution. The smallest penetration rate of MIGS into the bulk of GaAs is near the middle of the gap (midpoint) [9] with the characteristic length of $\sim 20$ Å. The penetration rate (decay rate) is
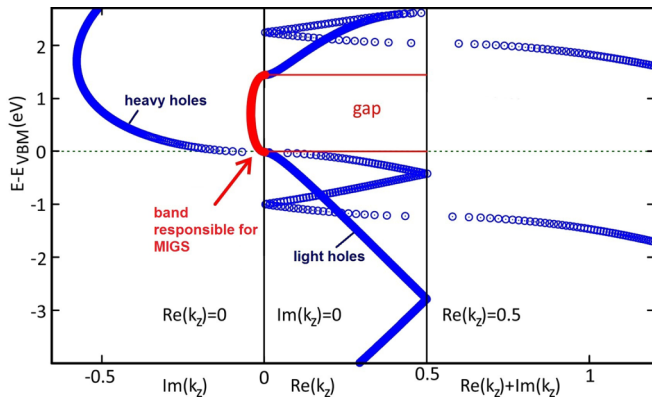
FIG. 7.  CBS $\kappa_z(E, k)$ of GaAs for (111) surface for $\Gamma$ point. The band highlighted by red (the slowest decaying band) corresponds to light holes and is responsible for evanescent states in the gap of the semiconductor.

increasing (decreasing) as the energy approaches VBM/CBM and diverges at the CBM/VBM ($\kappa_z = 0$).

### C. Surface of intrinsic GaAs

When the GaAs SC with $sp^3$ hybridization in the bulk is cleaved to create a surface, the dangling $sp^3$ bonds tend to form a surface with metallic properties [100]. The surface atoms tend to reconstruct to reduce the dangling bonds and minimize the surface energy [101–103]. The GaAs (111) surface is known to have several surface configurations [104]. One of the configurations with minimum surface energy is a $(2 \times 2)$ surface reconstruction with vacancies of the Ga atom [105–107]. In this configuration, on every $(2 \times 2)$ surface unit, one Ga atom is removed (see Figs. 8 and 9). The Ga vacancies in the surface layer create additional dangling bonds on the As atoms (dashed red lines in Fig. 8), which form pairs
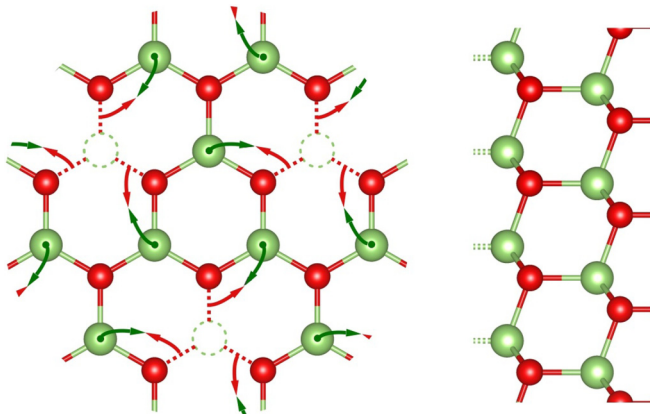


FIG. 8. Surface reconstruction $(2 \times 2)$ with vacancy of Ga (shown as dashed green circles) top view on the left, and cleaved surface of GaAs(111) side view on the right. The dangling bonds of Ga atoms exposed to vacuum are shown as green dots on the left and as dashed green lines on the right. The dangling bonds of As atoms are shown by dashed red lines. Dangling bonds of As-Ga tend to combine to eliminate all dangling bonds of the surface. The relaxed surface is shown on Fig. 9.
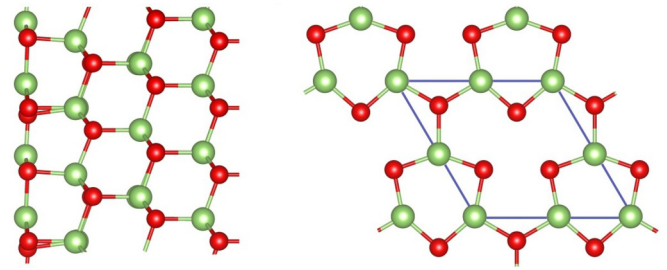


FIG. 9.  Relaxed flat surface GaAs (111) with $(2 \times 2)$ surface reconstruction with vacancy of Ga. Ga atoms in green, and As atoms in red. The left is the view along the $z$ direction perpendicular to the surface, and the right is the top view on the surface layer. Each $(2 \times 2)$ unit (shown as a blue quadrangle) has a vacancy of Ga.

with dangling bonds of Ga atoms exposed to vacuum [100] (see Fig. 8). Such a reconstruction favors relaxation of Ga atoms toward As atoms to form a planar surface with Ga-As $sp^2$ hybridized bonds [104]. Thus, after the reconstruction, the metallic character of the surface containing dangling bonds is changed back to a semiconducting character with all bonds filled. Such surface reconstruction creates surface states in the valence band and in the conduction band [108–111] which are partially filled (see Fig. 3) with the surface acceptor states at 0.27 eV above VBM [112].

We calculated the PDOS of the surface layer and the internal layers of the system containing six layers of GaAs. For intrinsic (undoped) GaAs, the Fermi level in the bulk is 0.78 eV (at 300 K) measured from the VBM, as determined from the total charge neutrality requirement. The Fermi level and intrinsic concentration of holes and electrons, which compensate each other in undoped GaAs, depend on the temperature [113].

On the surface, thermally activated surface holes in the surface valence band and electrons in the surface conduction band compensate each other to create the charge neutrality level (CNL) [7,9] on the surface. For undoped GaAs(111), the CNL coincides with the Fermi level of the bulk [104]. Thus, this surface is kept uncharged. However, some of the semiconducting surfaces may have slightly bent bands [5].

### D. Surface of doped GaAs

Doped SCs can be described simply by the location of the Fermi energy in the gap, which in turn determines the concentration of the carriers. By placing the Fermi energy at a desired energy in the calculation, we can adjust the doping level without dealing with the actual dopants. For example, for an $n$-type doped SC with a clean surface (i.e., not in contact with a metal or an overlayer), the surface layer exhibits electron accumulation filling the surface states, and the layers closer to the bulk have electrons depleted. This causes both the conduction and the valence bands to bend. The band bending moves the band gap away from the Fermi energy, affecting thermally activated holes and electrons.

In the bulk, doping, for example, with Si atoms as dopants substituting Ga atoms creates excess mobile electrons on
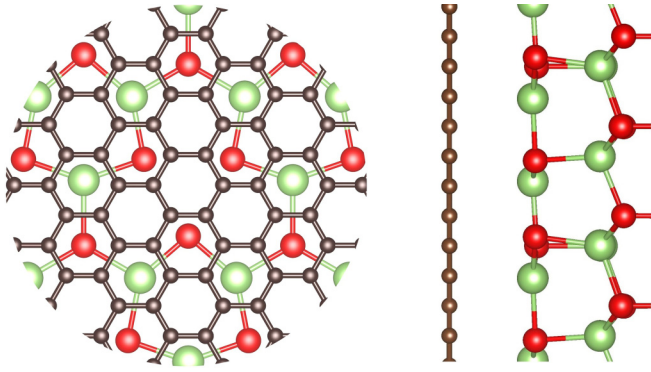
FIG. 10. GaAs(111) surface layer in contact with Gr, top view on the left (shown only Gr layer and surface layer of GaAs), Ga atoms in green, As atoms in red, and C atoms in gray. Ga and As atoms are placed against the hollow positions of Gr rings. On the right is the side view. The distance between the surface layer of GaAs and the Gr layer is 3.32 Å.

$Si_{Ga}$ defects which can freely move over the crystal. The typical resulting doping concentration with Si dopants is up to $10^{18}$ cm$^{-3}$ to $10^{20}$ cm$^{-3}$ [114]. The remaining body of positively charged defects $Si_{Ga}^{+}$ creates a compensating background charge, maintaining charge neutrality in the bulk.

### E. Surface of GaAs(111) in contact with graphene

Figure 10 shows the relaxed structure of GaAs(111)-Gr contact. Ga and As atoms are placed against the hollow positions of Gr rings. This structure corresponds to one of the possible minimum energy configurations [115]. The strain in the Gr layer is 6.3%. The structure was optimized in VASP using the exchange-correlation functional including the van der Waals correction. The relaxed distance between the surface of GaAs and the flat Gr layer is 3.32 Å.

Tables III and IV show the calculated SBH, the DLW, the ILW, the accumulated charge at the surface, and the electric field near the SC surface depending on the concentration for *n*-type (Table III) and *p*-type (Table IV) doping. The depletion layer appears due to band bending of the conduction band, whereas the inversion layer appears due to band bending of the valence band (see Fig. 3).

The characteristics of Schottky contact are sensitive to many parameters, like doping concentration and temperature. The self-consistent solution for the majority and minority carrier concentrations are also shown in Fig. 11 for *n*-type and in Fig. 12 for *p*-type doping, correspondingly. For Fermi level at CBM, the effective concentration of *n*-type doping is $1.15 \times 10^{17}$ cm$^{-3}$, and the depletion layer is 1014 Å, whereas the inversion layer is 9.2 Å. The charge accumulated at the surface is $1.11 \times 10^{12}$ cm$^{-2}$, and the SBH is 0.735 eV. Decreasing the Fermi level position or decreasing the concentration of *n*-type doping, the surface charge is also decreased, and the widths DLW and ILW are increased. The SBH is slightly decreased by 0.001 eV. For *p*-type doping concentration of $2.00 \times 10^{19}$ cm$^{-3}$, which corresponds to the Fermi level at VBM, the DLW is 74 Å and the ILW is 0.7 Å, whereas the SBH is 0.650 eV. Lowering the concentration of *p*-type doping (increasing the Fermi level), the SBH is increased, and the
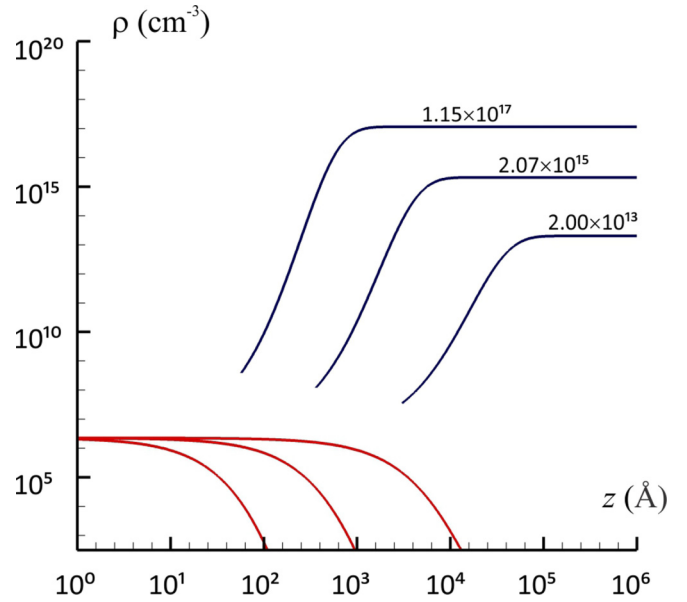


FIG. 11. Self-consistent solution for induced charge density of electrons (absolute value; blue) and holes (red) for $T = 300$ K, *n*-type doping with concentrations $\rho_n = 1.15 \times 10^{17}$ cm$^{-3}$, $2.07 \times 10^{15}$ cm$^{-3}$, and $2.00 \times 10^{13}$ cm$^{-3}$, respectively.

widths DLW and ILW are also increased. The SBH (Tables III and IV) are listed for *n*- and *p*-type doping, correspondingly.

The space charge layer width for GaAs experimentally measured by photothermal radiometric deep level transient spectroscopy ranges from 10 to 100 $\mu$m, depending on the treatment of the sample [112]. Calculated values of the DLW (Tables III and IV) are from $<100$ to $>10\,000$ Å, depending on doping concentration.
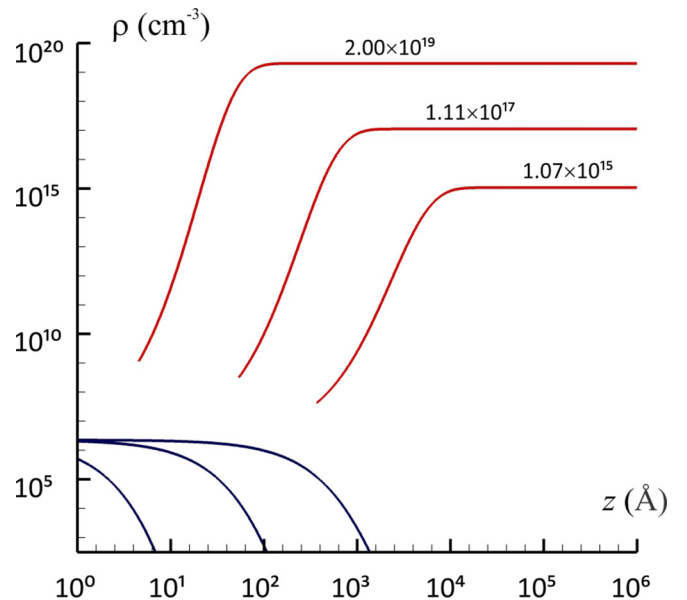


FIG. 12. Self-consistent solution for induced charge density of holes (red) and electrons (absolute value; blue) for $T = 300$ K, *p*-type doping with concentrations $\rho_p = 2.00 \times 10^{19}$ cm$^{-3}$, $1.11 \times 10^{17}$ cm$^{-3}$, and $1.07 \times 10^{15}$ cm$^{-3}$, respectively.

Tables V and VI show the dependence of SBH, DLW, ILW, $\sigma$, and electric field near the SC surface on temperature for *n*- and *p*-type doping, respectively. Increasing temperature reduces the depletion and ILWs due to increasing carrier concentration. This behavior shows qualitative agreement with experimental data for Au-GaAs measured by *I-V* curves [48].

## V. CONCLUSIONS

We have developed a first-principles theory for calculating SBH and the widths of depletion and inversion layers without using any empirical parameters. The theory is combining self-consistently the DFT calculations of the interface and the bulk layers under the influence of the electric field due to the Schottky potential, with the Poisson equation for the excess electrostatic potential due to charge redistribution on Schottky contact. The developed method is implemented in open-source software [116]. The method is tested on the GaAs(111)-Gr and Si(100)/Al(100) complexes. The depletion layer arises due to band bending of the conduction band, whereas the inversion layer arises due to band bending of the valence band. The SBH is a consequence emerging from the self-consistency between the redistributed charges in the bulk of the SC due to MIGS, thermally activated holes and electrons, and the electrostatic potential arising from these induced charges. We find that the SBH, the DLW, and the ILW depend on many factors, including temperature and doping concentration. The SBH is decreasing with increasing of the doping concentration because of filling of the surface states. We did not consider local inhomogeneities on the contact surfaces or local changes of the SBH due to doping atoms on the surface. The effects of electron tunneling through the Schottky barrier and thermionic field emission are also not included in our theory. Our method can have potential impact on modeling junctions where a Schottky barrier is present and allow one to compare experiments with first-principles calculations. This capability can be used to guide computational design of heterogeneous junctions. Further studies of GaAs-Gr with defects in the graphene layer and adsorbed atoms as well as a magnetic molecule-graphene-GaAs complex are underway.

## ACKNOWLEDGMENTS

## APPENDIX: INTEGRATION OVER k-SPACE

In parabolic approximation [117], the CBS decaying wave vector depends on $k_x$ and $k_y$ in the form

$$\kappa_z(E, k_r) = \sqrt{\kappa_z^2(E, 0) + k_r^2}, \qquad (A1)$$

where $k_r^2 = k_x^2 + k_y^2$.

At large distance, the PDOS is sharply peaked near $k_r = 0$; thus, we can approximate

$$\kappa_z(E, k_r) \approx \kappa_z(E, 0) + \frac{k_r^2}{2\kappa_z(E, 0)}. \qquad (A2)$$

This allows us to approximate the integrand in Eq. (17) by the Gaussian distribution

$$\exp\left(-\frac{k^2}{\delta^2}\right), \qquad (A3)$$

with a small width $\delta$:

$$D_i^{\mathrm{G}}(E, k_r, z) \approx D_i(E, 0, z) \exp\left[-\frac{k_r^2}{\kappa_z(E, 0)} z\right], \qquad (A4)$$

where

$$D_i(E, 0, z) = D_i(E, 0) \exp[-2\kappa_z(E, 0)z], \qquad (A5)$$

is the DOS of the interface distribution at $z$.

Using Eq. (A4), the integration over $d\mathbf{k}$ in Eq. (17) gives

$$D_{\mathrm{MIGS}}^{\mathrm{G}}(E, z) = D_i(E, 0) \exp\left[-2\kappa_z(E, 0)z\right] \frac{1}{\left(\frac{2\pi}{a}\right)^2} \frac{\kappa_z(E, 0)}{z}$$
$$\times \left\{1 - \exp\left[-\frac{\left(\frac{2\pi}{a}\right)^2}{\kappa_z(E, 0)} z\right]\right\}, \qquad (A6)$$

where $a$ is the lattice parameter.

The connection between numerical integration over $d\mathbf{k}$ in Eq. (17) and the analytical integration in Eq. (A6) can be made by comparison of the width of the Gaussian distribution for numerical and analytical solutions. The numerical solution is valid at small $z$, whereas the Gaussian solution is valid for $z$ far from the interface. The Gaussian parameter $\delta^2$ of Eq. (A4) is

$$\delta^2 = \frac{\kappa_z(E, 0)}{z}, \qquad (A7)$$

whereas the parameter $\delta^2$ of the numerical solution in Eq. (17) can be calculated numerically by several $k$-points close to $\Gamma$. Calculating the integrand in Eq. (17) at point $k^*$ and using Eq. (A3), we can write the Gaussian parameter $\delta^2$ for the numerical solution at the distance $z$ in the form

$$\delta^2 = \frac{k_*^2}{2z[\kappa_z(E, k_*) - \kappa_z(E, 0)] - \ln\left[\frac{D_i(E, k_*)}{D_i(E, 0)}\right]}. \qquad (A8)$$

The pure Gaussian distribution in Eq. (A7) has a parameter $\delta^2$ diverging at $z = 0$, whereas $\delta^2$ for the real distribution in Eq. (A8) has a finite value at $z = 0$ due to the Gaussian type distribution $D_i(E, \mathbf{k})$ near $\Gamma$ with a finite width at the interface.

Comparing Eq. (A8) with Eq. (A7) allows us to write the distance $z^*$ matching the two solutions:

$$z^* = \frac{-\ln\left[\frac{D_i(E, k_*)}{D_i(E, 0)}\right]}{\frac{k_*^2}{\kappa_z(E, 0)} - 2[\kappa_z(E, k_*) - \kappa_z(E, 0)]}. \qquad (A9)$$

[1] S. M. Sze and K. K. Ng, *Physics of Semiconductor Devices*, 3rd Ed. (John Wiley & Sons, New York, 2007).

[2] E. H. Rhoderick, The physics of Schottky barriers, J. Phys. D Appl. Phys. **3**, 1153 (1970).

[3] S. Ossicini, Theoretical approaches to the Schottky barrier problem, Appl. Surf. Sci. **56**, 290 (1992).

[4] R. T. Tung, Recent advances in Schottky barrier concepts, Mater. Sci. Eng. R **35**, 1 (2001).

[5] R. H. Williams, Interfaces in semiconductor structures and devices, Phys. Bl. **45**, 219 (1989).

[6] R. T. Tung, The physics and chemistry of the Schottky barrier height, Appl. Phys. Rev. **1**, 011304 (2014).

[7] J. Robertson, Band offsets, Schottky barrier heights, and their effects on electronic devices, J. Vac. Sci. Technol. A **31**, 050821 (2013).

[8] L. M. Porter and R. J. Hajzus, Perspectives from research on metal-semiconductor contacts: examples from $Ga_2O_3$, SiC, (nano)diamond, and SnS, J. Vac. Sci. Technol. A **38**, 031005 (2020).

[9] J. Tersoff, Theory of semiconductor heterojunctions: The role of quantum dipoles, Phys. Rev. B **30**, 4874 (1984).

[10] Y. Jiao, A. Hellman, Y. Fang, S. Gao, and M. Käll, Schottky barrier formation and band bending revealed by first-principles calculations, Sci. Rep. **5**, 11374 (2015).

[11] J. Michel, D. Splith, J. Rombach, A. Papadogianni, T. Berthold, S. Krischok, M. Grundmann, O. Bierwagen, H. von Wenckstern, and M. Himmerlich, Processing strategies for high-performance Schottky contacts on *n*-type oxide semiconductors: insights from $In_2O_3$, ACS Appl. Mater. Interfaces **11**, 27073 (2019).

[12] H. Hasegawa, T. Sato, and T. Hashizume, Evolution mechanism of nearly pinning-free platinum/*n*-type indium phosphide interface with a high Schottky barrier height by *in situ* electrochemical process, J. Vac. Sci. Technol. B **15**, 1227 (1997).

[13] H. H. Yoon, W. Song, S. Jung, J. Kim, K. Mo, G. Choi, H. Y. Jeong, J. H. Lee, and K. Park, Negative Fermi-level pinning effect of metal/*n*-GaAs(001) junction induced by a graphene interlayer, ACS Appl. Mater. Interfaces **11**, 47182 (2019).

[14] G.-S. Kim, S.-H. Kim, J. Park, K. H. Han, J. Kim, and H.-Y. Yu, Schottky barrier height engineering for electrical contacts of multilayered $MoS_2$ transistors with reduction of metal-induced gap states, ACS Nano **12**, 6292 (2018).

[15] P. W. Peacock and J. Robertson, Band offsets and Schottky barrier heights of high dielectric constant oxides, J. Appl. Phys. **92**, 4712 (2002).

[16] L. Jelver, D. Stradi, K. Stokbrob, and K. W. Jacobsen, Schottky barrier lowering due to interface states in 2D heterophase devices, Nanoscale Adv. **3**, 567 (2021).

[17] A. Latreche, Combined thermionic emission and tunneling mechanisms for the analysis of the leakage current for $Ga_2O_3$ Schottky barrier diodes, SN Appl. Sci. **1**, 188 (2019).

[18] Y.-H. Chen, C.-Y. Cheng, S.-Y. Chen, J.S.D. Rodriguez, H.-T. Liao, K. Watanabe, T. Taniguchi, C.-W. Chen, R. Sankar, F.-C. Chou, H.-C. Chiu, and W.-H. Wang, Oxidized-monolayer tunneling barrier for strong Fermi-level depinning in layered InSe transistors, npj 2D Mater. Appl. **3**, 49 (2019).

[19] P. A. Khomyakov, G. Giovannetti, P. C. Rusu, G. Brocks, J. van den Brink, and P. J. Kelly, First-principles study of the interaction and charge transfer between graphene and metals, Phys. Rev. B **79**, 195425 (2009).

[20] D. J. Chen, Y. Huang, B. Liu, Z. L. Xie, R. Zhang, Y. D. Zheng, Y. Wei, and V. Narayanamurti, High-quality Schottky contacts to alloys prepared for photovoltaic devices, J. Appl. Phys. **105**, 063714 (2009).

[21] L. J. Brillson and Y. Lu, ZnO Schottky barriers and Ohmic contacts, J. Appl. Phys. **109**, 121301 (2011).

[22] A. Vilan and D. Cahen, Chemical modification of semiconductor surfaces for molecular electronics, Chem. Rev. **117**, 4624 (2017).

[23] A. González-García, W. López-Pérez, R. González-Hernández, J. A. Rodríguez, M. V. Milošević, and F. M. Peeters, Tunable 2D-gallium arsenide and graphene bandgaps in a graphene/GaAs heterostructure: an *ab initio* study, J. Phys.: Condens. Matter **31**, 265502 (2019).

[24] K. Cheng, N. Han, Y. Su, J. Zhang, and J. Zhao, Schottky barrier at graphene/metal oxide interfaces: insight from first-principles calculations, Sci. Rep. **7**, 41771 (2017).

[25] K. Janicka, J. P. Velev, and Y. E. Tsymbal, Quantum Nature of Two-Dimensional Electron Gas Confinement at $LaAlO_3/SrTiO_3$ Interfaces, Phys. Rev. Lett. **102**, 106803 (2009).

[26] J. Betancourt, J. J. Saavedra-Arias, J. D. Burton, Y. Ishikawa, E. Y. Tsymbal, and J. P. Velev, Polarization discontinuity induced two-dimensional electron gas at ZnO/Zn(Mg)O interfaces: a first-principles study, Phys. Rev. B **88**, 085418 (2013).

[27] J. Betancourt, T. R. Paudel, E. Y. Tsymbal, and J. P. Velev, Spin-polarized two-dimensional electron gas at $GdTiO_3/SrTiO_3$ interfaces: Insight from first-principles calculations, Phys. Rev. B **96**, 045113 (2017).

[28] Y. Q. Cai, G. Zhang, and Y. W. Zhang, Layer-dependent band alignment and work function of few-layer phosphorene, Sci. Rep. **4**, 6677 (2014).

[29] D. O. Demchenko and A. Y. Liu, Influence of interface structure on electronic properties and Schottky barriers in Fe/GaAs magnetic junctions, Phys. Rev. B **73**, 115332 (2006).

[30] J. Chen, Z. Zhang, Y. Guo, and J. Robertson, Schottky barrier height at metal/ZnO interface: a first-principles study, Microelectron. Eng. **216**, 111056 (2019).

[31] Y. Takei and T. Nakayama, First-principles study of Schottky barrier behavior at metal/InN interfaces, Jpn. J. Appl. Phys. **48**, 081001 (2009).

[32] M. K. Niranjan, L. Kleinman, and A. A. Demkov, *Ab initio* study of atomic structure and Schottky barrier height at the $GaAs/Ni_{0.5}Pt_{0.5}Ge$ interface, Phys. Rev. B **77**, 155316 (2008).

[33] S. Picozzi, A. Continenza, G. Satta, S. Massidda, and A. J. Freeman, Metal-induced gap states and Schottky barrier heights at nonreactive GaN/noble-metal interfaces, Phys. Rev. B **61**, 16736 (2000).

[34] X. Liang, Y. Zhu, B. Peng, L. Deng, J. Xie, H. Lu, M. Wu, and L. Bi, Influence of interface structure on magnetic proximity effect in $Pt/Y_3Fe_5O_{12}$ heterostructures, ACS Appl. Mater. Interf. **8**, 8175 (2016).

[35] S. Ghosh, M. Baral, R. Kamparath, S. D. Singh, and T. Ganguli, Investigations on band commutativity at all oxide *p*-type NiO/*n*-type $\beta$-$Ga_2O_3$ heterojunction using photoelectron spectroscopy, Appl. Phys. Lett. **115**, 251603 (2019).

[36] N. H. Vu, H. V. Le, T. B. Phan, T. T. Nguyen, and N. Thoai, and T. M. Cao, Effect of surface states and breakdown of the Schottky-Mott limit of graphene/silicon van der Waals heterostructure, J. Phys. Chem. C **124**, 8958 (2020).

[37] S. Massidda, B. I. Min, and A. J. Freeman, Interface phenomena at semiconductor heterojunctions: local-density valence-band offset in GaAs/AlAs, Phys. Rev. B **35**, 9871 (1987).

[38] T. Nakayama, Valence band offset and electronic structures of zinc-compound strained superlattices, J. Phys. Soc. Jpn. **61**, 2434 (1992).

[39] C. Wang, L. Peng, Q. Qian, J. Du, S. Wang, and Y. Huang, Tuning the carrier confinement in GeS/phosphorene van der Waals heterostructures, Small **14**, 1703536 (2018).

[40] W. Mönch, Metal-semiconductor contacts: electronic properties, Surf. Sci. **299**, 928 (1994).

[41] A. J. Sambell and J. Wood, Unpinning the GaAs Fermi level with thin heavily doped silicon overlayers, IEEE Trans. Electr. Dev. **37**, 88 (1990).

[42] C. Tejedor, F. Flores, and E. Louis, The metal-semiconductor interface: Si (111) and zincblende (110) junctions, J. Phys. C Solid State Phys. **10**, 2163 (1977).

[43] J. Robertson, Band offsets of wide-band-gap oxides and implications for future electronic devices, J. Vac. Sci. Techn. B **18**, 1785 (2000).

[44] E. Dobrocka and J. Osvald, Influence of barrier height distribution on the parameters of Schottky diodes, Appl. Phys. Lett. **65**, 575 (1994).

[45] M. Stengel, P. Aguado-Puente, N. A. Spaldin, and J. Junquera, Band alignment at metal/ferroelectric interfaces: Insights and artifacts from first principles, Phys. Rev. B **83**, 235112 (2011).

[46] D. Stradi, U. Martinez, A. Blom, M. Brandbyge, and K. Stokbro, General atomistic approach for modeling metal-semiconductor interfaces using density functional theory and nonequilibrium Green's function, Phys. Rev. B **93**, 155302 (2016).

[47] A. J. Li, X. Zhu, D. Rhodes, C. C. Samouce, L. Balicas, and A. F. Hebard, Van der Waals Schottky barriers as interface probes of the correlation between chemical potential shifts and charge density wave formation in 1$T$-TiSe$_2$ and 2$H$-NbSe$_2$, Phys. Rev. B **96**, 125301 (2017).

[48] M. K. Hudait and S. B. Krupanidhi, Doping dependence of the barrier height and ideality factor of Au/n-GaAs Schottky diodes at low temperature, Phys. B **307**, 125 (2001).

[49] R. F. Broom, H. P. Meier, and W. Walter, Doping dependence of the Schottky barrier height of Ti-Pt contacts to $n$-gallium arsenide, J. Appl. Phys. **60**, 1832 (1986).

[50] V. W. L. Chin and M. S. Newbury, Determination of barrier height and doping density of a Schottky diode from infrared photoresponse measurements, Aust. J. Phys. **45**, 781 (1992).

[51] J. Tersoff, Schottky Barrier Heights and the Continuum of Gap States, Phys. Rev. Lett. **52**, 465 (1984).

[52] V. Heine, Theory of surface states, Phys. Rev. **138**, A1689 (1965).

[53] X.-G. Zhang and W. H. Butler, Band structure, evanescent states, and transport in spin tunnel junctions, J. Phys.: Condens. Matter **15**, R1603 (2003).

[54] J. Jiang, X.-G. Zhang, and X.-F. Han, Gap state charge induced spin-dependent negative differential resistance in

tunnel junctions, Lett. J. Explor. Front. Phys. **114**, 17005 (2016).

[55] G. Bordier and C. Noguera, Electronic structure of a metal-insulator interface: towards a theory of nonreactive adhesion, Phys. Rev. B **44**, 6361 (1991).

[56] R. G. Dandrea and B. C. Duke, Calculation of the Schottky barrier height at the Al/GaAs(001) heterojunction: effect of interfacial atomic relaxations, J. Vac. Sci. Technol. B **11**, 1553 (1993).

[57] M. Kiguchi, R. Arita, G. Yoshikawa, Y. Tanida, S. Ikeda, S. Entani, I. Nakai, H. Kondoh, T. Ohta, K. Saiki, and H. Aoki, Metal-induced gap states in epitaxial organic-insulator/metal interfaces, Phys. Rev. B **72**, 075446 (2005).

[58] V. Heine, On the general theory of surface states and scattering of electrons in solids, Proc. Phys. Soc. London **81**, 300 (1963).

[59] E. Prodan, Analytic structure of Bloch functions for linear molecular chains, Phys. Rev. B **73**, 035128 (2006).

[60] M. G. Reuter, A unified perspective of complex band structure: interpretations, formulations, and applications, J. Phys.: Condens. Matter **29**, 053001 (2017).

[61] X.-G. Li, I.-H. Chu, X.-G. Zhang, and H.-P. Cheng, Electron transport in graphene/graphene side-contact junction by plane-wave multiple-scattering method, Phys. Rev. B **91**, 195442 (2015).

[62] Y.-N. Wu, X.-G. Zhang, and T. S. Pantelides, First-principles calculations reveal controlling principles for carrier mobilities in semiconductors, Semicond. Sci. Technol. **31**, 115016 (2016).

[63] L. Zhang, P. Staar, A. Kozhevnikov, Y. P. Wang, J. Trinastic, T. Schulthess, and H. P. Cheng, DFT plus DMFT calculations of the complex band and tunneling behavior for the transition metal monoxides MnO, FeO, CoO, and NiO, Phys. Rev. B **100**, 035104 (2019).

[64] S. Tongay, M. Lemaitre, X. Miao, B. Gila, B. R. Appleton, and F. A. Hebard, Rectification at Graphene-Semiconductor Interfaces: Zero-Gap Semiconductor-Based Diodes, Phys. Rev. X **2**, 011002 (2012).

[65] S. Tongay, T. Schumann, and F. A. Hebard, Graphite based Schottky diodes formed on Si, GaAs and 4$H$-SiC substrates, Appl. Phys. Lett. **95**, 222103 (2009).

[66] J. P. Perdew, K. Burke, and M. Ernzerhof, Generalized Gradient Approximation Made Simple, Phys. Rev. Lett. **77**, 3865 (1996).

[67] E. P. Blöchl, Projector augmented-wave method, Phys. Rev. B **50**, 17953 (1994).

[68] T. Charpentier, The PAW/GIPAW approach for computing NMR parameters: A new dimension added to NMR study of solids, Sol. Stat. Nuc. Magn. Reson. **40**, 1 (2011).

[69] P. Giannozzi, O. Andreussi, T. Brumme, O. Bunau, M. Buongiorno Nardelli, M. Calandra, R. Car, C. Cavazzoni, D. Ceresoli, M. Cococcioni, N. Colonna, I. Carnimeo, A. Dal Corso, S. de Gironcoli, P. Delugas, R. A. DiStasio Jr, A. Ferretti, A. Floris, G. Fratesi, G. Fugallo *et al.*, Advanced capabilities for materials modelling with Quantum ESPRESSO, J. Phys.: Condens. Matter **29**, 465901 (2017).

[70] G. Kresse and J. Hafner, *Ab initio* molecular dynamics for liquid metals, Phys. Rev. B **47**, 558 (1993).

[71] G. Kresse and D. Joubert, From ultrasoft pseudopotentials to the projector augmented-wave method, Phys. Rev. B **59**, 1758 (1999).

[72] M. Dion, H. Rydberg, E. Schroder, D. C. Langreth, and B. I. Lundqvist, Van der Waals Density Functional for General Geometries, Phys. Rev. Lett. **92**, 246401 (2004).

[73] G. Roman-Perez and J. M. Soler, Efficient Implementation of a van der Waals Density Functional: Application to Double-Wall Carbon Nanotubes, Phys. Rev. Lett. **103**, 096102 (2009).

[74] J. Klimes, D. R. Bowler, and A. Michaelides, Chemical accuracy for the van der Waals density functional, J. Phys.: Condens. Mater **22**, 022201 (2010).

[75] Z. H. Levine and D. C. Allan, Linear Optical Response in Silicon and Germanium Including Self-Energy Effects, Phys. Rev. Lett. **63**, 1719 (1989).

[76] K. A. Johnson and W. N. Ashcroft, Corrections to density-functional theory band gaps, Phys. Rev. B **58**, 15548 (1998).

[77] Y. Xu, C. Cheng, S. Du, J. Yang, B. Yu, J. Luo, W. Yin, E. Li, S. Dong, P. Ye, and X. Duan, Contacts between two- and three-dimensional materials: Ohmic, Schottky, and *p-n* Heterojunctions, ACS Nano **10**, 4895 (2016).

[78] J. M. Wilkinson, J. D. Wilcock, and M. E. Brinson, Theory and experiment for silicon Schottky barrier diodes at high current density, Solid-State Electron. **20**, 45 (1977).

[79] N. M. Namordi and H. W. Thomson, Aluminum-silicon Schottky barriers as semiconductor targets for EBS devices, Solid-State Electron. **18**, 499 (1975).

[80] A. Y. C. Yu and C. A. Mead, Characteristics of aluminum-silicon Schottky barrier diode, Solid-State Electron. **13**, 97 (1970).

[81] H. C. Card, Aluminum-silicon Schottky barriers and ohmic contacts in integrated circuits, IEEE Trans. Electr. Dev. ED **23**, 538 (1976).

[82] A. Thanailakis, Contacts between simple metals and atomically clean silicon, J. Phys. C Solid State Phys. **8**, 655 (1975).

[83] B. L. Smith and E. H. Rhoderick, Schottky barriers on *p*-type silicon, Solid State Electron. **14**, 71 (1971).

[84] B. Pellegrini, New quantum and electronic theory of metal-semiconductor contacts, Phys. Rev. B **7**, 5299 (1973).

[85] B. Pellegrini, A detailed analysis of the metal-semiconductor contact, Solid-State Electron. **17**, 217 (1974).

[86] F. García-Moliner and J. Rubio, The quantum theory of one-electron states at surfaces and interfaces, Proc. R. Soc. Lond. **324**, 257 (1971).

[87] E. Louis, F. Yndurain, and F. Flores, Metal-semiconductor junction for (110) surfaces of zinc-blende compounds, Phys. Rev. B **13**, 4408 (1976).

[88] J. Osvald and E. Dobrocka, Generalized approach to the parameter extraction from *I-V* characteristics of Schottky diodes, Semicond. Sci. Technol. **11**, 1198 (1996).

[89] C. Poole and I. Darwazeh, Microwave semiconductor materials and diodes, in *Microwave Active Circuit Analysis and Design* (Academic Press, 2015).

[90] C. Manfredotti and K. K. Sharma, On the role of inversion layer, electronic density of states and interfacial layer on the barrier height formation of amorphous-silicon Schottky diodes, MRS Online Proc. Library **118**, 463 (1988).

[91] H. B. Yao, D. Z. Chi, R. Li, S. J. Lee, and D.-L. Kwong, Effect of the inversion layer on the electrical characterization of Pt germanide/Schottky contacts, Appl. Phys. Lett. **89**, 242117 (2006).

[92] T. M. Wijesinghe and M. Premaratne, Surface plasmon polaritons propagation through a Schottky junction: influence of the inversion layer, IEEE Photonics J. **5**, 4800216 (2013).

[93] G. Shoute, A. Afshar, T. Muneshwar, K. Cadien, and D. Barlage, Sustained hole inversion layer in a wide-bandgap metal-oxide semiconductor with enhanced tunnel current, Nature Comm. **7**, 10632 (2016).

[94] W. S. dos Santos, M. Rodriguez, A. S. Afonso, J. P. Mesquita, L. L. Nascimento, A. O. T. Patrocínio, A. C. Silva, L. C. A. Oliveira, J. D. Fabris, and M. C. Pereira, A hole inversion layer at the $BiVO_4/Bi_4V_2O_{11}$ interface produces a high tunable photovoltage for water splitting, Sci. Rep. **6**, 31406 (2016).

[95] A. Di Bartolomeo, G. Luongo, F. Giubileo, N. Funicello, G. Niu, T. Schroeder, M. Lisker, and G. Lupina, Hybrid graphene/silicon Schottky photodiode with intrinsic gating effect, 2D Mater. **4**, 025075 (2017).

[96] E. Demoulin and F. van de Wiele, Inversion layer at the interface of Schottky diodes, Solid State Electron. **17**, 825 (1974).

[97] K. K. Sharma, Influence of thin inversion layers on Schottky diodes, Rev. Phys. Appl. (Paris) **21**, 25 (1986).

[98] J. R. Brews, A charge-sheet model of the MOSFET, Solid State Electron. **21**, 345 (1978).

[99] A. Smogunov, A. Dal Corso, and E. Tosatti, Ballistic conductance of magnetic Co and Ni nanowires with ultrasoft pseudopotentials, Phys. Rev. B **70**, 045417 (2004).

[100] D. J. Chadi and M. L. Cohen, Intrinsic (111) surface states of Ge, GaAs, and ZnSe, Phys. Rev. B **11**, 732 (1975).

[101] D. J. Chadi, Vacancy-Induced $2 \times 2$ Reconstruction of the GaAs(111) Surface of GaAs, Phys. Rev. Lett. **52**, 1911 (1984).

[102] S. G. Louie, J. R. Chelikowsky, and M. L. Cohen, Theory of semiconductor surface states and metal-semiconductor interfaces, J. Vac. Sci. Technol. **13**, 790 (1976).

[103] D. K. Biegelsen, R. D. Bringans, J. E. Northrup, and L. E. Swartz, Reconstruction of GaAs(111) Surfaces Observed by Scanning Tunneling Microscopy, Phys. Rev. Lett. **65**, 452 (1990).

[104] D. A Woolf, D. I. Westwood, and R. H. Williams, Surface reconstructions of GaAs(111)A and (111)B: A static surface phase study by reflection high-energy electron diffraction, Appl. Phys. Lett. **62**, 1370 (1993).

[105] E. Kaxiras, Y. Bar-Yam, J. D. Joannopoulos, and K. C. Pandey, *Ab initio* theory of polar semiconductor surfaces. I. Methodology and the $(2 \times 2)$ reconstructions of GaAs(111), Phys. Rev. B **35**, 9625 (1987).

[106] S. Y. Tong, G. Xu, and W. N. Mei, Vacancy-Buckling Model for the $(2 \times 2)$ GaAs(111) Surface, Phys. Rev. Lett. **52**, 1693 (1984).

[107] A. Ohtake, J. Nakamura, T. Komura, T. Hanada, T. Yao, H. Kuramochi, and M. Ozeki, Surface structures of GaAs{111}A,B-$(2 \times 2)$, Phys. Rev. B **64**, 045318 (2001).

[108] J. R. Chelikowsky and M. L. Cohen, Self-consistent pseudopotential calculation for the relaxed (110) surface of GaAs, Phys. Rev. B **20**, 4150 (1979).

[109] D. J. Chadi, (110) surface states of GaAs: Sensitivity of electronic structure to surface structure, Phys. Rev. B **18**, 1800 (1978).

[110] M. Enachea, C. Negrilab, M. Anastasescua, G. Dobrescua, M. F. Lazarescub, and V. Lazarescua, Surface states and

field-effects at GaAs(100) electrodes in sodium dodecyl sulfate acid solution, J. Electrochem. Soc. **165**, H3008 (2018).

[111] W. G. Schidt, F. Bechstedt, and J. Berholc, GaAs(001) surface reconstructions: Geometries, chemical bonding and optical properties, Appl. Surf. Science **190**, 264 (2002).

[112] A. Mandelis and R. A. Budiman, Evidence of a surface acceptor state in undoped semi-insulating GaAs by photothermal radiometric deep level transient spectroscopy, Superf. y Vacio **8**, 13 (1999).

[113] M. Shur, *Physics of semiconducting devices* (Prentice-Hall, Englewood Cliffs, 1990).

[114] J. E. Northrup and S. B. Zhang, Dopant and defect energetics: Si in GaAs, Phys. Rev. B **47**, 6791 (1993).

[115] A. M. Munshi, D. L. Dheeraj, V. T. Fauske, D.-C. Kim, A. T. J. van Helvoort, B.-O. Fimland, and H. Weman, Vertically aligned GaAs nanowires on graphite and few-layer graphene: generic model and epitaxial growth, Nano Lett. **12**, 4570 (2012).

[116] Available on GitHub at https://github.com/m2qm-efrc/SB.

[117] X. Guan, D. Kim, K. C. Saraswat, and H. S. P. Wong, Complex band structures: from parabolic to elliptic approximation, IEEE Electr. Device Lett. **32**, 1296 (2011).